NEUROSCIENCE

Eukaryotic Kv channel Shaker inactivates through selectivity filter dilation rather than collapse

Robyn Stix[1,2]†, Xiao-Feng Tan[3]†, Chanhyung Bae[3], Ana I. Fernández-Mariño[3], Kenton J. Swartz[3]*, José D. Faraldo-Gómez[1]*

Eukaryotic voltage-gated K^+ channels have been extensively studied, but the structural bases for some of their most salient functional features remain to be established. C-type inactivation, for example, is an auto-inhibitory mechanism that confers temporal resolution to their signal-firing activity. In a recent breakthrough, studies of a mutant of Shaker that is prone to inactivate indicated that this process entails a dilation of the selectivity filter, the narrowest part of the ion conduction pathway. Here, we report an atomic-resolution cryo–electron microscopy structure that demonstrates that the wild-type channel can also adopt this dilated state. All-atom simulations corroborate this conformation is congruent with the electrophysiological characteristics of the C-type inactivated state, namely, residual K^+ conductance and altered ion specificity, and help rationalize why inactivation is accelerated or impeded by certain mutations. In summary, this study establishes the molecular basis for an important self-regulatory mechanism in eukaryotic K^+ channels, laying a solid foundation for further studies.

INTRODUCTION

Voltage-activated potassium (Kv) channels open and close in response to changes in membrane voltage, serving critical functions in excitable cells such as neurons and muscle, as well as non-excitable cells where they are involved in ion homeostasis (*1*, *2*). The Shaker Kv channel was the first K^+ channel to be cloned, and subsequent functional studies of that channel have been foundational for establishing key mechanistic principles that are relevant for different types of K^+ channels, as well as voltage-activated sodium (Nav) channels and voltage-activated calcium (Cav) channels (*1*, *3*–*5*). In the Shaker Kv channel, membrane depolarization leads to outward movement of the Arg-rich S4 helix within peripheral S1 to S4 voltage-sensing domains and subsequent opening of the internal pore where the activation gate resides within the pore-lining S6 helix (*1*, *3*–*6*). However, opening of the Shaker Kv channel is transient because the channel rapidly inactivates on the timescale of milliseconds through a mechanism wherein the N terminus is thought to plug the internal pore through a ball-and-chain mechanism (*7*–*10*). The Shaker Kv channel also slowly inactivates on the timescale of seconds through a mechanism termed C-type inactivation (*11*), which diminishes the availability of Kv channels to open, regulating the firing of action potentials in neurons and cardiac muscle and has been implicated in neurological and psychiatric disorders (*1*, *12*–*15*). The human ether-a-go-go-related Kv channel also rapidly enters a C-type inactivated state, underlying the unique inwardly rectifying properties of the channel that are critical for shaping the cardiac action potential and preventing arrhythmias (*16*–*19*). Conformational changes related to C-type inactivation also serve important roles in Ca^{2+}-activated K^+ channels and K2P channels (*20*, *21*).

It has long been hypothesized that C-type inactivation in Shaker Kv channels involves a conformational change in the ion selectivity filter within the external pore. This reasoning followed the observation that inactivation is influenced by mutations in this region as well as by ion and blocker occupancy of the selectivity filter (*11*, *14*, *15*, *22*–*34*). Until recently, the prevailing view has been that this conformational change entails the constriction or collapse of the ion selectivity filter. This notion was originally proposed on the basis of engineered Cd^{2+} bridges in Shaker and supported by x-ray structures of the KcsA channel, a model prokaryotic K^+-selective channel that consists of a pore domain homologous to that found in Kv channels (*35*–*37*). However, the notion of selectivity filter collapse has been questioned (*15*) and is hard to reconcile with the observation of residual K^+ conductance and increased Na^+ permeability following C-type inactivation (*30*). A recent structure of the Shaker Kv channel containing the W434F mutation, which strongly promotes slow C-type inactivation (*23*, *29*, *38*, *39*), revealed that the ion selectivity filter actually dilates during C-type inactivation (*40*), leading to the selective loss of K^+ ion binding sites within the external half of the filter. A highly similar loss of K^+ ion binding sites within the conduction pore has also been observed in K2P channels (*41*), a family of K^+ channels for which the selectivity filter had been long thought to be an important gate. In contrast to a collapsed state, which would entirely preclude ion conduction, a dilated conformation would be more congruent with the observation that the inactivated state remains permeable. Consistently, dilation of the ion selectivity filter has also been recently reported for the Kv1.2/2.1 paddle chimera containing mutations that promote inactivation (*42*), as well as for the Kv1.3 channel from T lymphocytes (*43*, *44*). Despite this evidence, a recent study has suggested that the inactivated state promoted by the W434F mutation might be distinct from that accessed by the wild-type (WT) channel (*45*). To resolve this controversy, in the present study, we set out to experimentally determine the structure of the WT Shaker Kv channel in a C-type inactivated state without using inactivation-promoting

[1]Theoretical Molecular Biophysics Laboratory, National Heart, Lung and Blood Institute, National Institutes of Health, Bethesda, MD 20892, USA. [2]Department of Biology, Johns Hopkins University, 3400 N. Charles Street, Baltimore, MD 21218, USA. [3]Molecular Physiology and Biophysics Section, Porter Neuroscience Research Center, National Institute of Neurological Disorders and Stroke, National Institutes of Health, Bethesda, MD 20892, USA.
*Corresponding author. Email: swartzk@ninds.nih.gov (K.J.S.); jose.faraldo@nih.gov (J.D.F-.G.)
†These authors contributed equally to this work.

mutations. We also used molecular dynamics (MD) simulations to contrast the known electrophysiological characteristics of the C-type inactivated state with the conductive properties of existing structures of WT and mutagenized Shaker. Our experimental and computational findings provide strong support to the notion that dilation of the ion selectivity filter is indeed the mechanism of C-type inactivation and provide the foundation for future mechanistic and pharmacological studies.

RESULTS AND DISCUSSION

Structure of the WT Shaker Kv channel in lipid nanodiscs in low K^+

In our original structure of the Shaker Kv channel determined in 150 mM K^+, the ion selectivity filter adopts the conducting conformation that is typical of this family of K^+ channels (*40*). This result was expected, as high external K^+ stabilizes the conducting state of the channel and slows entry into the C-type inactivated conformation (*24*). Following this observation, we reasoned that a structure determined using low concentrations of K^+ might instead reveal the C-type inactivated state, without any mutations of the channel. To pursue this hypothesis, we expressed the full-length WT Shaker Kv channel (*7*, *8*) containing an mVenus tag in mammalian cells, purified and reconstituted the protein into lipid nanodiscs using MSP1E3D1 (*46*) in 150 mM K^+ and then exchanged the solution to one containing 4 mM K^+. To evaluate the structure of the channel in these conditions, we used cryo–electron microscopy (cryo-EM) (fig. S1 and table S1). After focused refinement, the cryo-EM data enabled us to determine the structure of the transmembrane domain of WT Shaker at 2.39-Å resolution; the map is of high quality throughout, with clearly resolved densities for most side chains, making de novo atomic model building straightforward. Only the two external loops within the voltage-sensing domains are poorly resolved (residues H254 to T276 and V330 to M356), as is the intracellular domain, and therefore, these regions were not modeled. Although we anticipated that studies of the full-length WT channel might also reveal insights into mode of interaction of the N terminus with the internal pore and therefore into as-yet-unknown mechanism of N-type inactivation (*7*, *8*), no density that could be attributed to the N terminus was evident in our cryo-EM maps.

As in the previous structures determined in high K^+, the structure of WT Shaker in low K^+ features the voltage-sensing domains in an activated state, and accordingly, the intracellular S6 gate region (*47*) is open. Examination of the ion selectivity filter within the external pore, however, reveals that WT Shaker in low K^+ adopts a conformation that is markedly different from that observed at high K^+ yet largely indistinguishable from that stabilized by the W434F mutation (Fig. 1). For both the W434F mutant at high K^+ and WT Shaker in low K^+, there is an overall reorganization of side-chain interactions behind the filter in the inactivated state, with critical residues within the P-loop between Y445 and P450 undergoing substantial displacements. The key interaction between D447 in the P-loop and W434 in the pore helix, observed in the activated state of Shaker and other K^+ channels (*6*, *38*, *48*), is disengaged in low K^+ despite the presence of W434, resulting in a displacement of the P-loop toward the external solution by about 5 Å (Fig. 1). At the external end of the ion selectivity filter, the side chain of Y445 undergoes a major reorientation in low K^+, breaking off its hydrogen bond contact with T439 in the adjacent subunit and rotating 90° to reposition behind the filter of the same subunit (Fig. 1). As in the W434F mutant, the reorganization seen for the WT Shaker channel in low K^+ translates into a marked expansion by ~4 Å at the external portion of the ion selectivity filter (Fig. 1), perturbing the ion densities therein without altering those within the internal end of the filter (Fig. 1). The structure of WT Shaker in low K^+ therefore corroborates that its selectivity filter can adopt a state distinct from the conductive conformation, which entails pronounced yet highly localized structural changes, and that is remarkably similar to what we previously reported for the W434F mutant (*40*). Given that both the W434F mutation and the low K^+ condition foster C-type inactivation, it is logical to conclude that these cryo-EM structures capture the inactivated state of the channel.

Filter dilation explains residual conductance of C-type inactivated state

To independently ascertain whether dilation of selectivity filter is indeed the mechanism of C-type inactivation of Shaker, we sought to evaluate the basic conducting properties of this conformation, using all-atom MD simulations. However, to provide a baseline for this analysis and calibrate the accuracy of our methodology, we first evaluated the K^+ conductance of the activated state and compared known experimental values with simulation results obtained under similar conditions. The results of this evaluation for activated WT Shaker are summarized in Figs. 2 and 3. Upon application of 300 mV across the membrane, positive on the intracellular side, the simulation showed steady outward K^+ flow (Fig. 2A). Specifically, in a 10-μs window, we observed 66 permeation events, which translate into a single-channel conductance of 3.5 pS. Outward ion flow could also be observed at 100 mV (Fig. 2B), although in the same 10-μs period, we detected much fewer permeation events. Experimental single-channel recordings have shown that the conductance of Shaker in symmetric 300 mM KCl, which is also the simulated condition, is approximately 30 pS (*49*). Our simulation design thus underestimates the K^+ permeation rate, but only by a factor of 10, which is satisfactory in our view, given the myriad approximations inherent to this kind of calculation, most of which are necessary to maximize the statistical quality of the results. The mechanisms of K^+ permeation at 100 and 300 mV appear largely identical (Figs. 2, C and D, and 3 and movies S1 and S2). Consistent with what has been described in other simulation studies of K^+ flow (*50*), three K^+ ions typically occupy the selectivity filter. In the condition examined in our simulation, the outermost binding site is the most labile, and external K^+ ions are seen to occasionally exchange there, while the other two K^+ ions in the filter are effectively stationary. With some frequency, an additional K^+ ion approaches the cavity formed under the selectivity filter by helices S5 and S6 via the open cytoplasmic gate. These incoming K^+ ions often return to the bulk without any discernible effect, but with some probability, they cause the outermost ion in the filter to unbind; in such instances, the central and innermost K^+ ions move outward, driven by the applied electric field, and the cavity ion enters the filter, returning the channel to the initial state (Figs. 2, C and D, and 3 and movies S1 and S2). This resetting is rapid and highly concerted and is completed within a few tens of nanoseconds; outward ion flow thus appears to be limited by the rate at which the outermost ion binding site becomes vacant. A revealing difference between the simulations at 100 and 300 mV is the

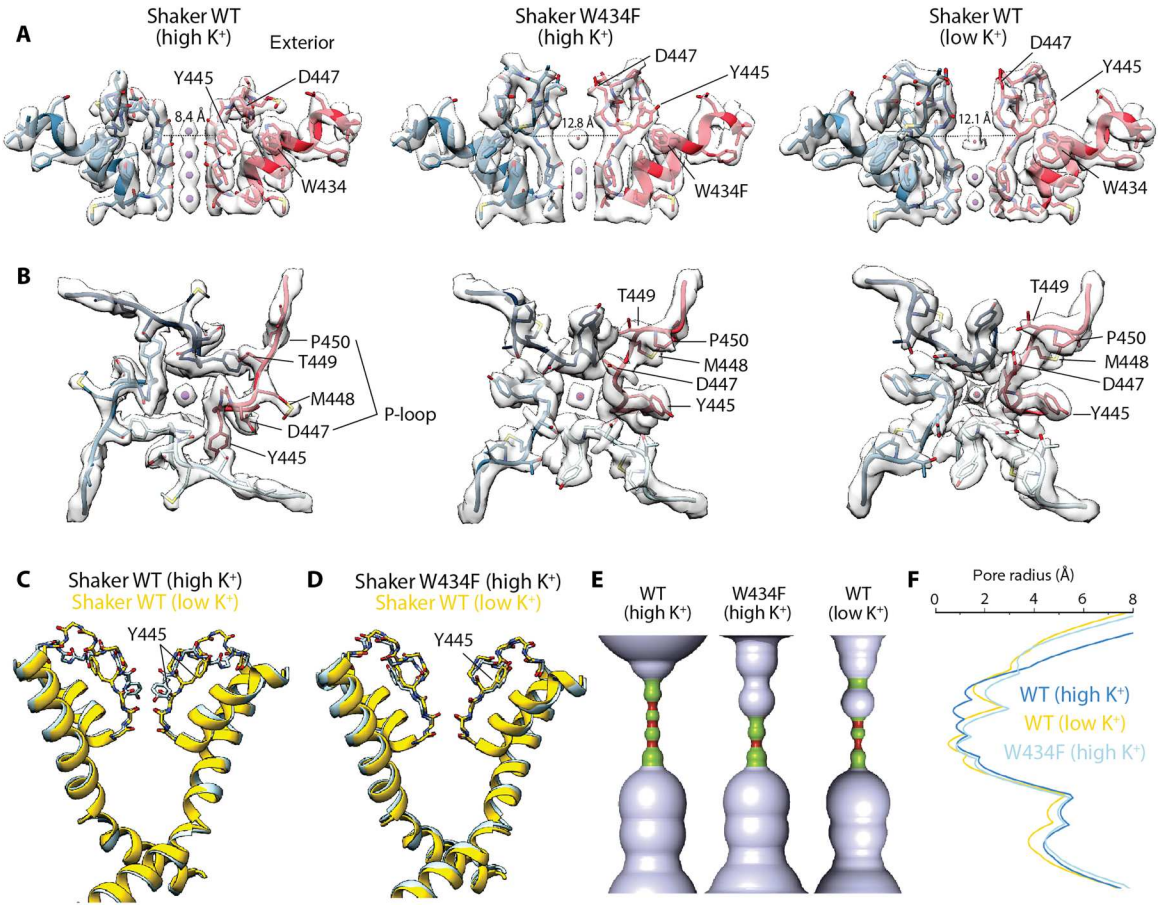

Fig. 1. Structures of the external pore of WT Shaker in high K^+, W434F Shaker in high K^+, and WT Shaker in low K^+. (**A**) Side views of the ion selectivity filter in the structures of WT Shaker in high K^+ (left), W434F Shaker in high K^+ (middle), and WT Shaker in low K^+ (right). Note the two high K^+ structures are of the so-called Shaker-IR (N-type Inactivation Removed) construct, which lacks the N terminus, while that at low K^+ is of the full-length channel. The distance between Y445 CA indicates the degree of dilation of selectivity filter. Key residues displaced in the conformational change are represented with sticks. (**B**) Same as (A), with the selectivity filter viewed from the outside. (**C**) Superposition of the pore-lining regions of Shaker in the WT structures obtained at high and low K^+. The reorientation of residue Y445, shown with sticks, is highlighted. (**D**) Superposition of the pore-lining regions of Shaker in the W434F structure in high K^+ and the WT structure in low K^+. (**E**) Graphical illustration of the change in pore radius along the ion permeation pathway, for WT Shaker in high K^+ (left), W434F Shaker (middle), and WT Shaker in low K^+ (right). Regions with radii of ≤1 Å are colored in red, those with radii of >1 and ≤2 Å are colored in green, those with radii of >2 Å are colored in light blue. (**F**) Numerical quantification of the data represented in (E), for the same conformations.

likelihood with which K^+ ions reside in the cavity; because the transmembrane potential gradient begins inside this cavity, in the latter condition, K^+ ions are over five times more likely to approach the selectivity filter (Fig. 2E), explaining why the knock-on mechanism described above is initiated more frequently. Last, it is worth noting that, at times, K^+ ions entering the filter from the cavity retain one of the water molecules in their hydration shell, which then codiffuses across the channel alongside the ion (fig. S2); however, most of the observed permeation events, particularly at 100 mV, did not involve water-mediated interactions between the K^+ ions, in line with the results of de Groot and co-workers (*51*). It is also worth noting that while our simulations represent the channel and its lipid membrane environment in atomic detail, they include only the pore domain and not the voltage sensors. This simplification enabled us to consider a molecular system of smaller dimensions and therefore study ion flow for a longer period of simulated time. To preclude changes in the functional state of the channel that might result from this truncation, we introduced a modification in the energy function that biases the dynamics of the channel so that, on average, it approximately maintains the structure observed experimentally (throughout the pore domain) while permitting appropriate fluctuations both at the level of the side chains and the backbone (Materials and Methods and fig. S3). This approach ensures that the cytoplasmic gate remains open despite the absence of the sensors (fig. S3D); however, on the basis of an analogous analysis of a full-length K^+ channel highly similar to Shaker (not shown), we anticipate that K^+ ions would be channeled into the cavity more efficiently if the sensors were present. If so, the throughput rate across the filter would be accelerated, bringing the calculated conductance estimate even closer to experimental values.

Having calibrated the expected accuracy of our simulation design for the activated state, we applied the same methodology to study the dilated state, in both the WT structure reported in this study and the W434F structure reported previously. The results are shown in Fig. 4. To directly compare with the active-state simulation, we first applied a 300-mV voltage, but over a 2-

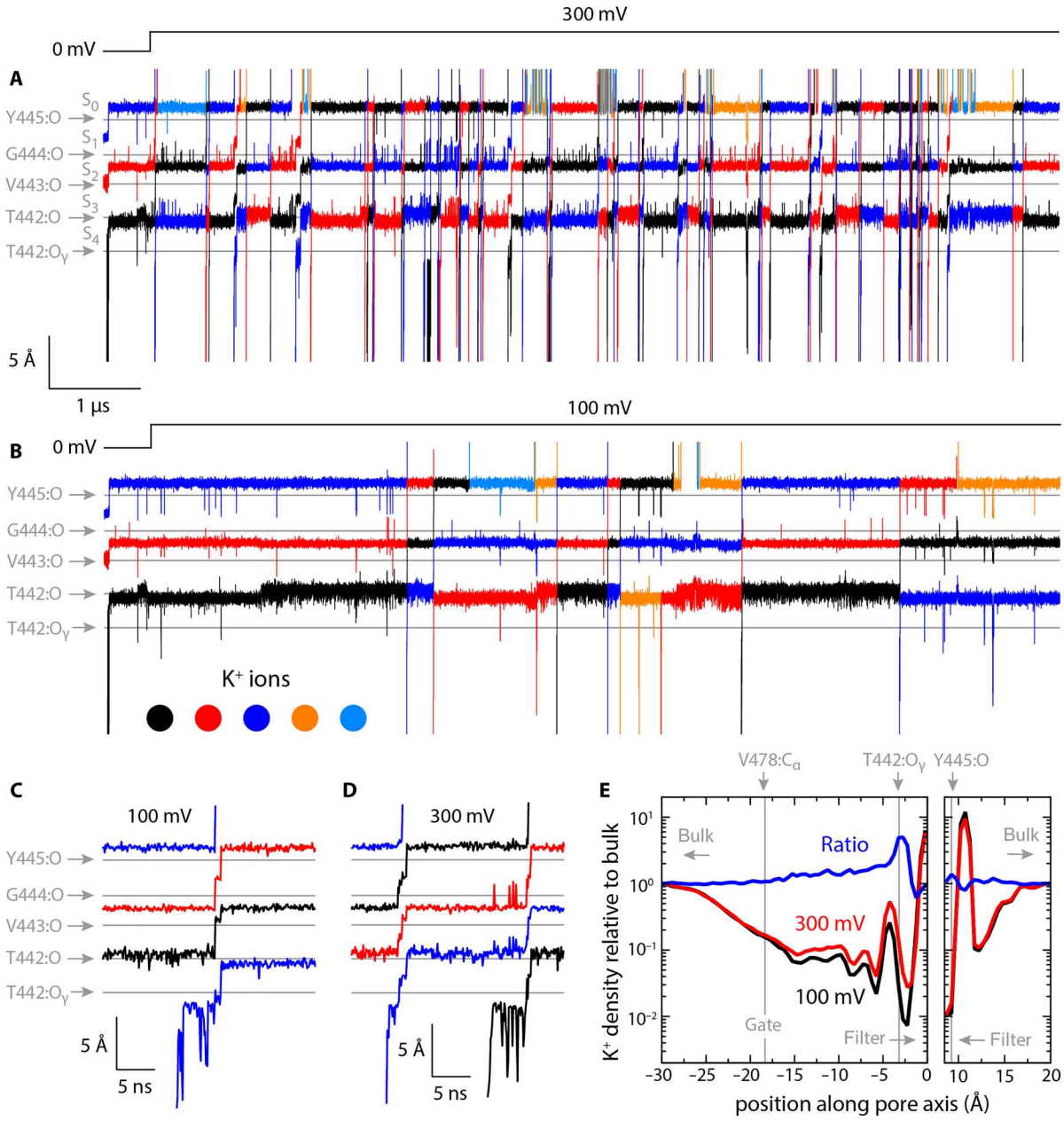

Fig. 2. Rate and mechanism of outward K^+ permeation in MD simulations of activated Shaker. (**A**) Time series of the position of K^+ ions as they traverse (black/red/blue) or transiently enter (orange, light blue) the selectivity filter. The relative average positions of coordinating backbone/side-chain oxygens in residues 442 to 445 are indicated, along with the site nomenclature used in previous studies. Note that K^+ trajectories are only represented if the ion ultimately enters the filter. Also note that no voltage was applied during the first 0.5 µs of the trajectory; a jump to 300 mV was introduced at this point and sustained for 10 µs thereafter. (**B**) Same as (A), for a jump to 100 mV, also sustained for 10 µs. (**C**) Representative permeation event at 100 mV, depicted with greater temporal resolution to reveal the knock-on mechanism. (**D**) Same as (C), for two sequential permeation events at 300 mV. (**E**) K^+ density along the axis of the channel, relative to the bulk value, up until the cytosolic entrance of the selectivity filter (left plot) and beyond the extracellular exit (right plot). Data are superposed for the 100 and 300 mV conditions (black and red), and the ratio is shown to highlight the differences (blue). The average positions of residues marking the cytosolic gate (V478) and the entrance and exit of the selectivity filter (T442 and Y445, respectively) are indicated.

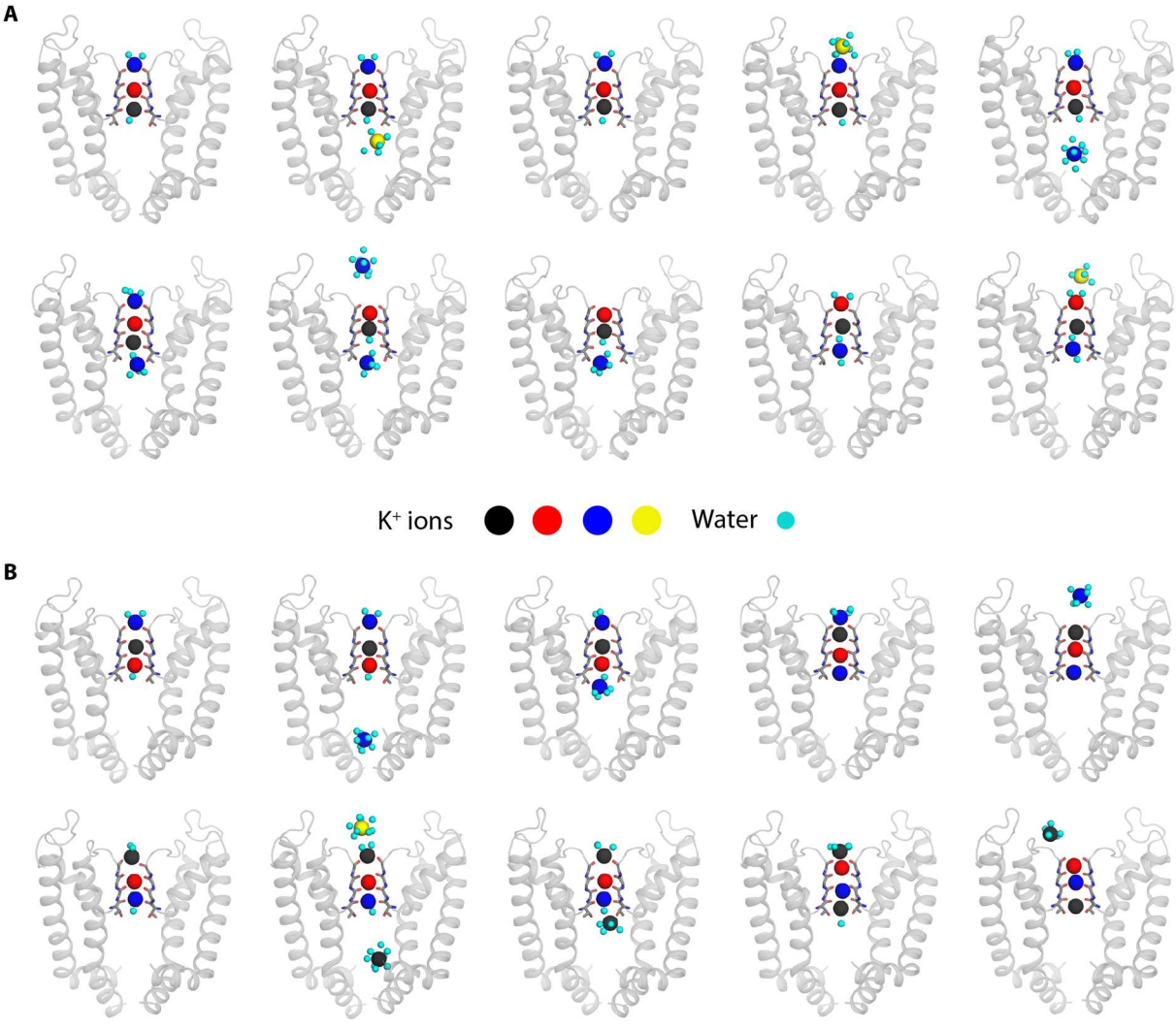

Fig. 3. Mechanism of K^+ permeation in MD simulations of activated Shaker. (**A**) Sequential snapshots of the permeation event depicted in Fig. 2C, at 100 mV. K^+ ions are color-coded as in the time traces (black/blue/red). Additional K^+ ions approaching the filter from either side are also shown (yellow), as are water molecules in the first hydration shell of any K^+ ion. The channel is shown as gray cartoons, except for the ion-coordinating groups in the selectivity filter. Two of the channel subunits are omitted, as are the surrounding lipid bilayer and the solvent. (**B**) Same as (A), for the two permeation events depicted in Fig. 2D, at 300 mV.

μs window, we detected no permeation events in either case (Fig. 4, A and B). Upon increase to 450 mV, however, we observed sustained ion flux outward, for both structures, albeit at a much slower rate than for the activated state (Fig. 4, A and B), and with a different mechanism. We observe that dilation of the filter effectively eliminates the two outermost ion binding sites, and thus, this permeation mechanism involves at most two K^+ ions in the filter (Fig. 4, C and D, and movie S3). As in the activated state, cytosolic K^+ ions can readily enter the cavity via the open gate, but these events do not seem sufficient to dislodge the outermost K^+ ion from the filter. Thus, outward permeation stalls until this site is spontaneously vacated; only then can the innermost ion move outward, and the cavity ion enter the filter, quite rapidly (Fig. 4, C and D, and movie S3). Dilated WT and W434F appear highly similar in these simulations and show an approximate conductance of 0.3 pS. That is, these simulations show that the dilated filter is permeable but about one order of magnitude less so than the activated state. As mentioned above, experimental electrophysiological recordings reveal that Shaker generates macroscopic K^+ currents of detectable magnitude following C-type inactivation, specifically about 5% of that observed for the activated state (*30*). Taken alone, these data could be interpreted as reflecting an equilibrium between a majority population of entirely nonconducting channels (e.g., with a collapsed filter) and a minority population of normally conducting channels. However, this interpretation would not explain why the Na^+ permeability of Shaker increases in the C-type inactivated state (*30*). Instead, the most plausible explanation for the existing electrophysiological data is that C-type inactivation reflects a growing population of channels with distinct conducting properties, for example, reduced K^+ permeability. The 20-fold reduction on K^+ conductance compares well with our simulation results, lending support to the theory that dilation of the selectivity filter is indeed the mechanism of C-type inactivation of this channel.

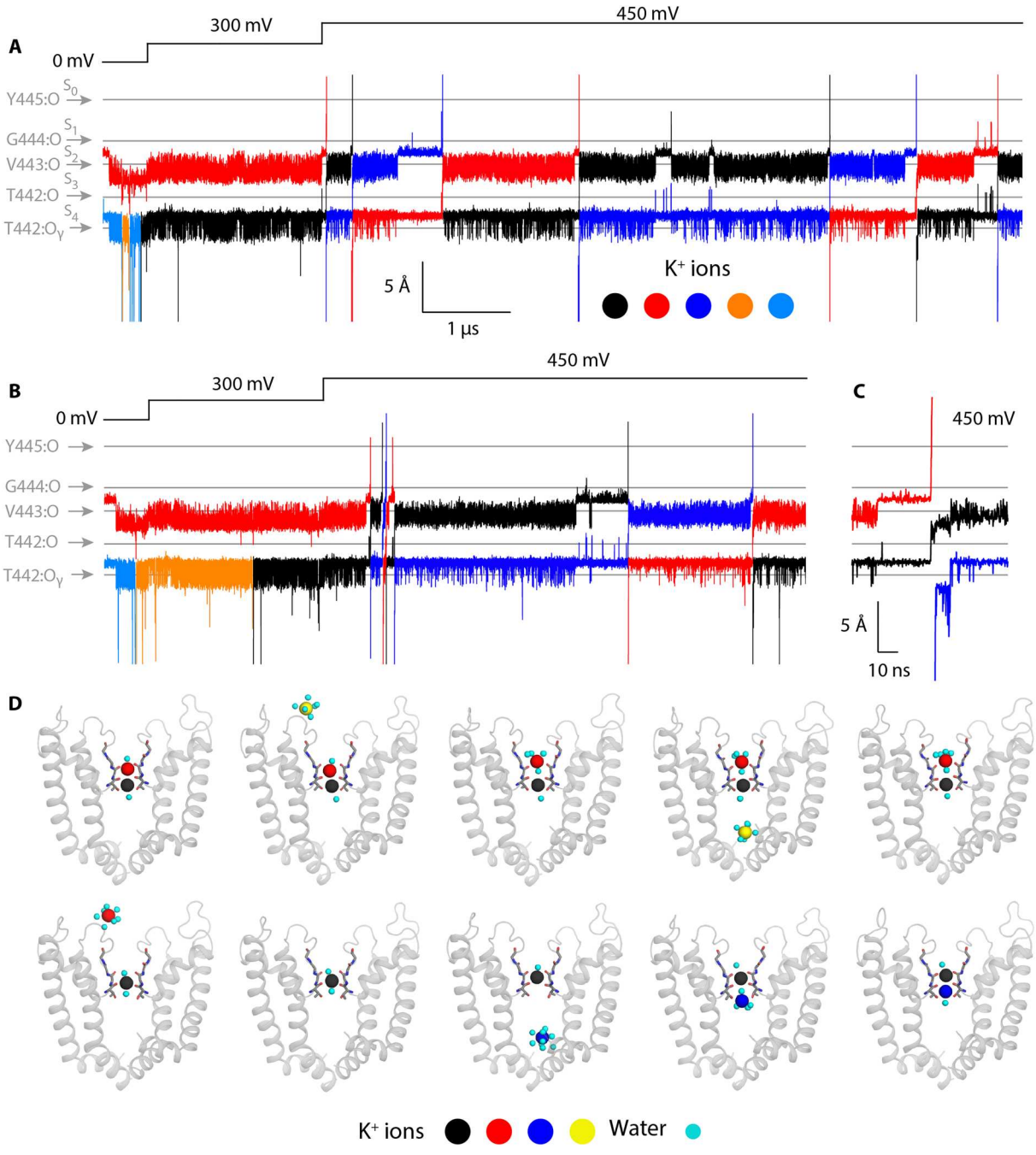

Fig. 4. Rate and mechanism of outward K^+ permeation in MD simulations of C-type inactivated Shaker. (**A**) Time series of the position of K^+ ions as they traverse (black/red/blue) or transiently enter (orange, light blue) the selectivity filter, in simulations of the W434F mutant with a dilated selectivity filter. The relative average positions of coordinating backbone/side-chain oxygens in residues 442 to 445 are indicated, along with the site nomenclature used in previous studies. Note that K^+ trajectories are only represented if the ion ultimately enters the filter. Also note that no voltage was applied during the first 0.5 µs of the trajectory; a jump to 300 mV was introduced at this point, and after 2 µs, a second jump was made to 450 mV, which was sustained for 8 µs. (**B**) Same as (A), for simulations of the WT channel with a dilated filter, based on the cryo-EM structures reported in this study. (**C**) Representative permeation event in the latter simulation, depicted with greater temporal resolution to reveal its mechanism. (**D**) Sequential snapshots of the permeation event depicted in (C). K^+ ions are color-coded as in the time traces (black/blue/red). Additional K^+ ions approaching the filter from either side are also shown (yellow), as are water molecules in the first hydration shell of any K^+ ion. The channel is represented as in Fig. 3.

Filter dilation is consistent with altered ion selectivity of C-type inactivated state

As mentioned above, C-type inactivation causes Shaker to be more permeable to Na^+, and while K^+ is still the preferred ion, the channel becomes less selective relative to the activated state (*30*). While precise quantitative comparisons of Na^+ throughput rates are unfeasible at this time, we reasoned that microsecond-timescale simulations designed to probe the competition between K^+ and Na^+ for binding to the channel could further support (or refute) the notion that filter dilation is the mechanism of C-type inactivation in Shaker. To that end, we extended the simulations reported above for WT activated and dilated states at 300 mV in 300 mM KCl (Figs. 2A and 4, A and B), after exchanging the buffer to a mixture of 150 mM KCl and 150 mM NaCl. The results of these simulations are summarized in Fig. 5. Because the simulations include equal concentrations of K^+ and Na^+, both ions approach either side of the filter with comparable probability, irrespective of its conformation (Fig. 5, A and B). Before the buffer exchange, only K^+ ions reside in the filter, but outward movement of these ions eventually permit a Na^+ ion in the cavity to bind to the innermost site, in both the activated and dilated states (Fig. 5, C and D, and movies S4 and S5). As expected, we do not observe further ion flux in the 10-μs timescale for either state, but the interplay of ions with activated and dilated structures differs clearly otherwise. In the activated filter, we observe reversible binding and unbinding of both K^+ and Na^+ at the outermost site. K^+ is preferred in this competition, although, and so under these conditions, Na^+ tends to coexist with two K^+ ions on the central and outermost sites (Figs. 5C and 6A). In clear contrast, when Na^+ enters the dilated filter (from the intracellular side), the two K^+ ions initially bound therein are displaced completely (Figs. 5D and 6B and movies S4 and S5). Examination of the mode of interaction between these ions and the dilated filter provides a rationale for this result. As has been noted elsewhere (*52*), while K^+ ions are most stable near the center of cages formed by eight carbonyl groups (Fig. 4D), Na^+ prefers instead to align with a plane formed by the central four carbonyl groups (Fig. 6B). Thus, Na^+ binding to the center of the dilated filter precludes K^+ occupancy of either of the two sites that remain in this conformation, as it would entail a prohibitive electrostatic repulsion with the Na^+ ion. Together, these simulation data clearly indicate that dilation of the filter alters the nature of the competition between K^+ and Na^+, in a manner that appears to favor the latter cation. The observation that Na^+ can occupy the dilated filter without K^+ suggests that this state is more naturally permeable to Na^+ than the activated state, which is not prone to bind Na^+ alone if K^+ is present in comparable concentrations. In conclusion, while at this time we cannot evaluate Na^+ throughput rates, this preliminary examination of the ion selectivity of Shaker provides additional support to the notion that the dilated filter reflects the C-type inactivated state of this channel. On the basis of this finding, it is now possible to design additional simulation studies to examine the mechanism of Na^+ permeation across the active and inactive states of the channel and to quantify its ion selectivity in either case.

Insights into the energetic factors controlling C-type inactivation

As mentioned, the simulations of Shaker reported above were designed to evaluate the functional characteristics of each of the channel structures that have been experimentally determined. To do so, the force field used in these simulations was supplemented with an additional energy term that precludes major conformational changes—specifically in ϕ, ψ, and χ_1 dihedral angles—while permitting substantial local fluctuations around the experimental geometry (Materials and Methods and fig. S3). By construction, therefore, no interconversion between activated and inactivated states can take place in the course of the calculated trajectories. C-type inactivation, however, is a spontaneous process, and so we wondered whether a simulation of the activated state in which the selectivity filter is permitted to change conformation freely would reveal insights into the onset of this inactivation mechanism. The result of this simulation is shown in Figs. 7 and 8. As expected, we observed no K^+ flow in the initial 0-mV condition, which lasted 500 ns (Fig. 7A); during this time, three K^+ ions occupy the filter, which remained in the activated state (Fig. 8A). No significant changes were observed upon stepping up the potential to 300 mV, for about 700 ns. At that point, however, K^+ time traces indicate a conformational change that eliminates the outermost binding sites and that precludes ion flux for the reminder of the trajectory, 5.5 μs in total (Fig. 7A). Analysis of the simulated trajectory confirms that this conformational change indeed occurs (Fig. 8A) and shows that its onset is the disengagement of the hydrogen bond between the side chains of D447 and W434 (Fig. 8, B and C). Specifically, D447 rotates toward the extracellular space, where it becomes fully hydrated, causing the flanking residues to adjust their configuration. The most significant adjustment is in the main chain of Y445, whose carbonyl group rotates about 100° away from the center of the conduction pathway, although its side chain remains hydrogen bonded to T439 (fig. S4). Subtle adjustments are also observed for G444 and V443, but overall, the configuration of the cytosolic half of the filter is largely unchanged, as are the hydrogen bonding interactions that seem to support it (Fig. 8, B and C, and fig. S4). Another change worth noting on the extracellular space is the formation of a hydrogen bond between the side chain of T449 and the backbone of D447, which does not exist in the activated state (Fig. 8, B and C).

These changes do not fully capture the extent of the differences between the cryo-EM structures of the activated and inactivated states; most notably, we do not observe a reconfiguration of the side chain of Y445, whose displacement and rotation ultimately cause the dilation of the filter (Fig. 8C). Nonetheless, there are clear similarities otherwise, most notably the rotation of D447 and the elimination of the outermost binding sites, which suggest that this simulation might be revealing the early steps in the C-type inactivation process (Fig. 8C). That the disengagement of the D447 and W434 initiates this transition would be consistent with the fact that C-type inactivation in Shaker is strongly accelerated by the W434F mutation (which cannot engage D447); it also seems clear that rotation of D447 must precede the reconfiguration of Y445, as otherwise these side chains would occupy the same space (Fig. 8C). In addition, that T449V in the background of W434F rescues ion conduction (*28*, *53*) would be consistent with the observation that the T449 hydroxyl (not available in T449V) engages the D447 backbone in a hypothetical intermediate (Fig. 8, B and C).

On the other hand, it is certainly a concern that these spontaneous changes occur only about 1 μs of simulation. That is, it is problematic that the lifetime of the activated state in a simulated trajectory whereby the filter dynamics is entirely unrestricted is

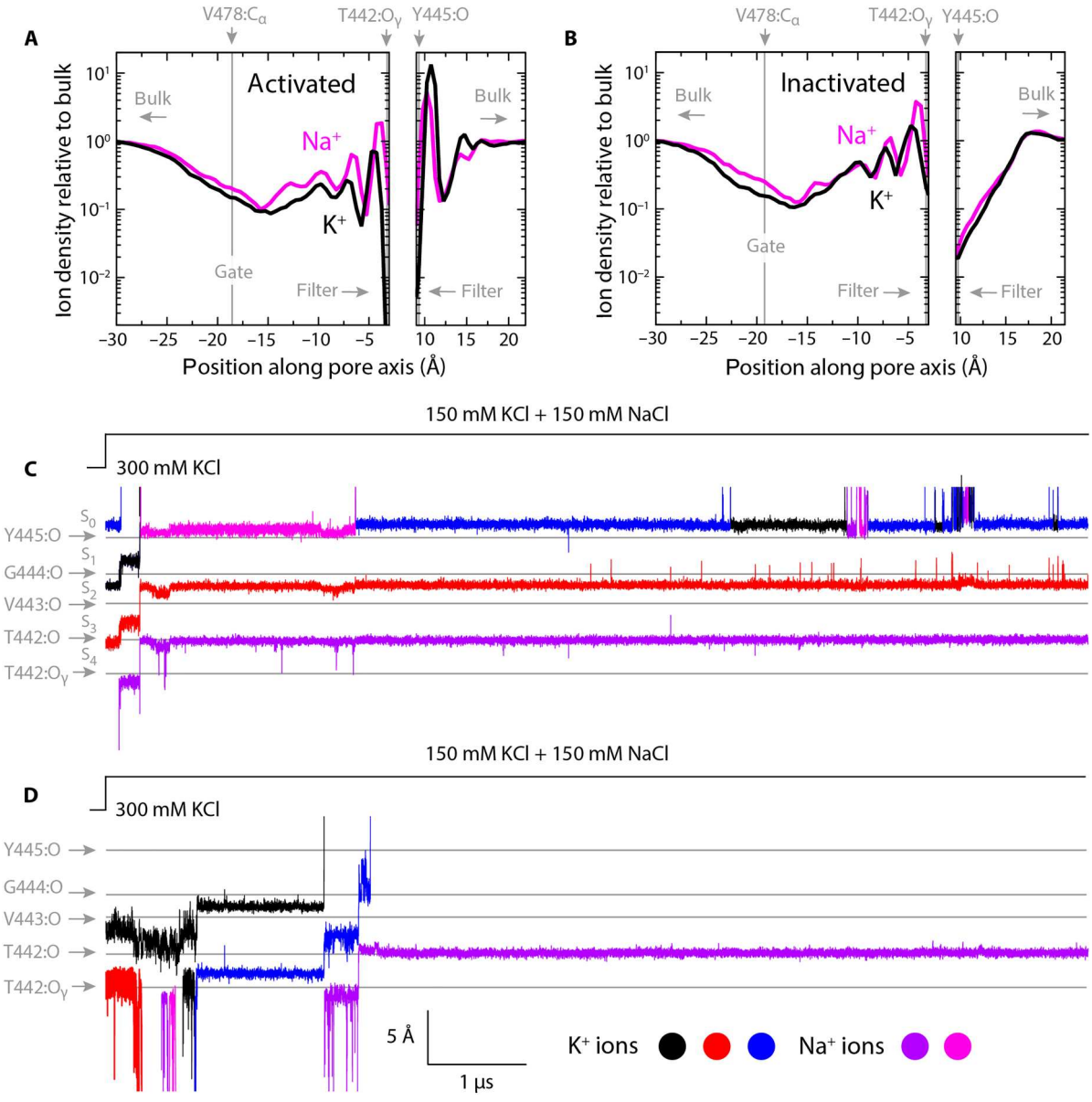

Fig. 5. Ion selectivity of activated and C-type inactivated Shaker in MD simulations. Data are shown for trajectories with an applied 300-mV voltage and equal concentrations of KCl and NaCl. (**A** and **B**) Density of K^+ and Na^+ (black and magenta) along the axis of the channel, relative to their respective bulk values, up until the cytosolic entrance of the selectivity filter (left plot) and beyond the extracellular exit (right plot). The average positions of residues marking the cytosolic gate (V478) and the entrance and exit of the selectivity filter (T442 and Y445, respectively) are indicated. (**C** and **D**) Time series of the positions of K^+ (black/red/blue) and Na^+ ions (purple/magenta) as they enter and/or reside in the selectivity filter, in simulations of the activated (C) or the C-type inactivated state (D). The relative positions of coordinating backbone/side-chain oxygens in residues 442 to 445 are indicated alongside. Note that ion trajectories are only represented if the ion ultimately enters the filter.

multiple orders of magnitude shorter than the characteristic time of the C-type inactivation process (*11*). In other words, while the structural changes described above appear to be meaningful, it is also clear that their onset is artificially accelerated. A likely explanation is that the force field used in our simulations (CHARMM36m) does not accurately capture the strength of the hydrogen bond between D447 and W434. The strength of this type of interaction depends on the value of the partial electronic charges assigned by the simulation force field to each of the atoms involved. These charges, however, are typically optimized to best represent the hydrated state of the amino acid and might not be adequate for a different chemical environment. For example, the interaction between D447 and W434 is likely to induce a significant amount of electronic polarization in both the carboxyl group and the indole ring, i.e., a redistribution of the atomic charges, relative to the hydrated state, which will strengthen the interaction. The force field used in our simulations does not capture polarization effects, i.e., atomic charges are constant not adaptive. If such effects were included, it is highly probable that dissociation of D447 from W434 would be delayed and that the structural

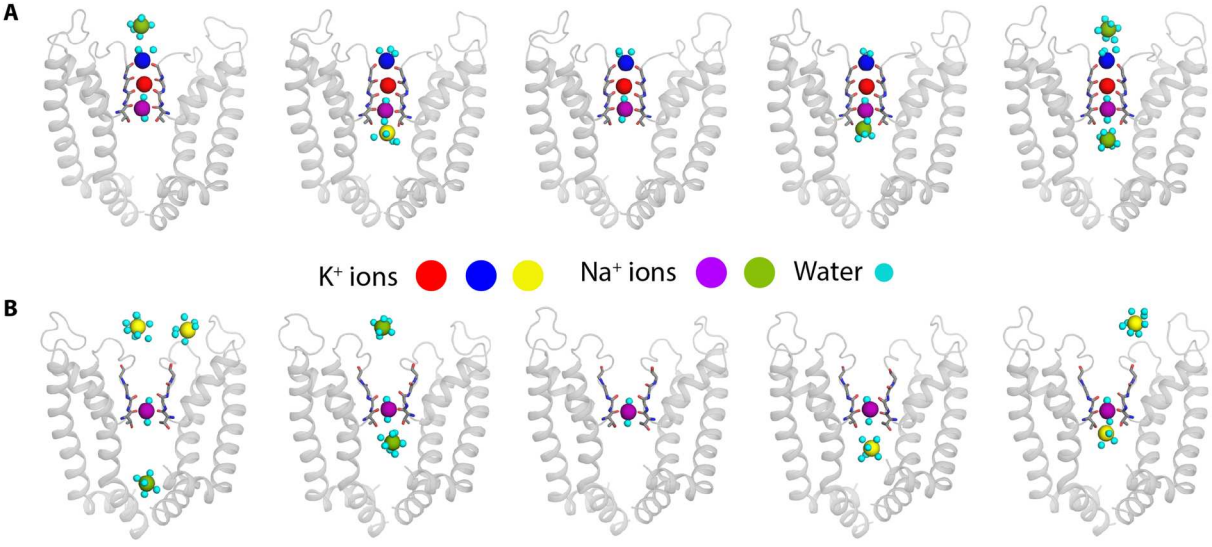

Fig. 6. Ion selectivity of activated and C-type inactivated Shaker in MD simulations. (**A**) Sequential snapshots of the competition between K^+ and Na^+ depicted in Fig. 5C, for activated Shaker. K^+ and Na^+ ions are color-coded as in the time traces (black/blue/red, purple/magenta). Additional K^+ and Na^+ ions approaching the filter from either side are also shown (yellow/green), as are water molecules in the first hydration shell of any K^+ or N^+ ion. The channel is represented as in Fig. 3. (**B**) Same as (A), for the trajectory depicted in Fig. 5D for the C-type inactivated state.

changes in the filter described above would occur in a more realistic timescale. To corroborate this interpretation, we conducted another simulation in which the selectivity filter was again unrestricted, but in which the hydrogen bonds between D447 and W434 were preserved throughout, in the four channel subunits (Materials and Methods). This simulation showed no conformational changes in the filter, which remained in the activated state (Fig. 8 and fig. S4). Accordingly, the simulation also showed K^+ permeation, at a rate and mechanism comparable to those observed in the simulation in which the activated configuration of the filter was more explicitly maintained by controlling the ϕ, ψ, and χ_1 dihedral angles (Figs. 2 and 7B).

Despite their paramount biomedical significance and decades of extensive study, the molecular mechanisms of most classes of ion channels remain to be fully understood. Functional and structural studies have revealed much about the mechanisms by which channels activate in response to changes in transmembrane voltage, temperature, the availability of certain ligands, or the state of the membrane. However, the physiological activity of most ion channels is actually the result of a complex series of processes, among which activation is only the first step. Many ion channels spontaneously inactivate soon after opening, i.e., they undergo structural changes that ultimately inhibit or eliminate ion flow. Inactivation is a crucial physiological feature, in that it confers a temporal resolution to the signaling activity of a given channel, irrespective of the activation stimuli. It can be therefore thought of as a self-regulatory mechanism. Just as crucial is the process often referred to as recovery from inactivation, i.e., a subsequent structural change that restores the channel to a conductive state. Paradoxically, recovery oftentimes requires elimination of the activation stimuli, i.e., channel closing.

The molecular world is governed by the laws of statistical thermodynamics, and therefore, the only adequate framework to rationalize ion channel mechanisms is that of free-energy landscapes. In this perspective, activation, inactivation, and recovery are evidence that the free-energy landscape of an ion channel is not constant; instead, it evolves as the channel progresses from one functional state to another, increasing the probability of structural changes that were previously improbable while precluding others. The precise timescale and nature of these changes will vary from channel to channel, reflecting different cellular requirements. Nevertheless, it seems clear that mapping these free-energy landscapes, and elucidating the factors the explain their evolution, is the next frontier in ion channel research. To do so, it will be crucial to first identify the series of structural states accessed by a channel during its functional cycle, with the highest possible precision. In the case of eukaryotic Kv channels such as Shaker, elucidation of the atomic structures of both the activated and the C-type inactivated states is, in our view, a necessary milestone toward a more complete and rigorous understanding of the molecular basis of ion channel physiology.

MATERIALS AND METHODS

WT Shaker Kv channel expression using Baculovirus-mammalian cell expression systems

To initiate structural studies of inactivation in the Shaker Kv channel, the full-length WT channel was cloned into the pEG vector in which enhanced green fluorescent protein was substituted with mVenus (*54*) and expressed in tsA201 cells using the previously published Baculovirus-mammalian expression system with a few minor modifications (*55*). Briefly, P1 virus was generated by transfecting Sf9 cells (~2.5 million cells on a T25 flask with a vent cap) with 50 to 100 ng of fresh Bacmid using Cellfectin. After 4 to 5 days of incubation in a humidified 28°C incubator, the cell culture medium was collected by centrifugation (3000*g* × 10 min), supplemented with 2% fetal bovine serum (FBS), and filtered through a 0.45-μm filter to harvest the P1 virus. To amplify the P1 virus,

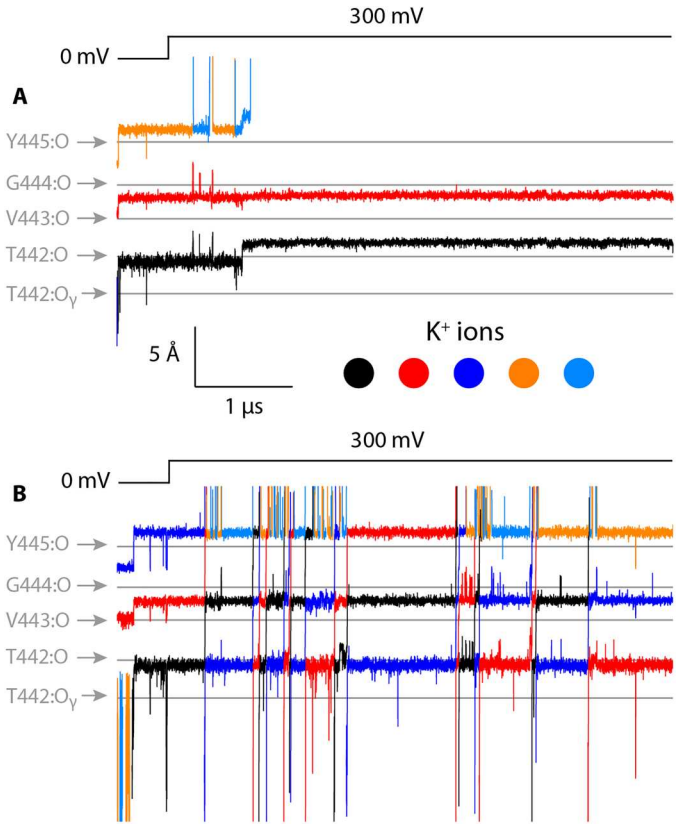

Fig. 7. MD simulations of activated Shaker using alternative protocols. (**A**) Same as Fig. 2A, for a simulation in which the dynamics of the selectivity filter (residues 440 to 447) is free of any biases or restraints, i.e., only determined by the simulation force field (Materials and Methods). (**B**) Same as (A) for a simulation in which the dynamics of the selectivity filter is free of any biases or restraints, but the following hydrogen bonding interactions are preserved throughout: D447 to W434, T441 to V437, and T439 to Y445 (Materials and Methods).

~500 ml of Sf9 cell cultures at a ~1.5 million cells/ml density was infected with 1 to 200 µl of the virus and incubated in a 28°C shaking incubator for 3 days. The cell culture media was then collected by centrifugation (5000*g* × 20 min), supplemented with 2% FBS, and filtered through 0.45-µm filter to harvest P2 virus. The volume of P1 virus used for the amplification was determined by carrying out a small-scale amplification screening in which ~10 ml of Sf9 cell cultures at the same density was infected with different volume of P1 virus and harvested after 3 days to transduce tsA201 cells and compare the expression level of WT Shaker Kv channels using mVenus fluorescence intensity. The P2 virus was protected from light using aluminum foil and stored at 4°C until use. To express the Shaker channels, tsA201 cells at ~1.5 million cells/ml in Freestyle medium with 2% FBS were transduced with 10% (v/v) P2 virus and incubated at a 37°C CO_2 incubator. To boost the protein expression, sodium butyrate (2 M stock in H_2O) was added to 10 mM at ~16 hours of posttransduction. The culture was continued at the 37°C CO_2 incubator for another 24 hours, and the cells were harvested by centrifugation (5000*g* × 20 min) and frozen at −80°C until use.

WT Shaker Kv channel purification

Before extraction of the Shaker Kv channels from tsA201 cells, membrane fractionation was carried out using a hypotonic solution and ultracentrifugation. The cells were first resuspended in a hypotonic solution [20 mM tris (pH 7.5) and 10 mM KCl] with protease inhibitors [pepstatin, aprotinin, leupeptin, benzamidine, trypsin inhibitor, and phenylmethylsulfonyl fluoride (PMFS)] using a Dounce homogenizer, incubated at 4°C for ~30 min, and centrifuged at 1000*g* for 10 min to remove cell debris. The supernatant was ultracentrifuged for 1 hour (45,000 rpm, Beckman Ti45 rotor), and collected membranes were stored at −80°C until use. To purify WT Shaker Kv channels, the fractionated membranes were resuspended in an extraction buffer [50 mM tris (pH 7.5), 150 mM KCl, 2 mM Tris(2-carboxyethyl)phosphine hydrochloride (TCEP), 50 mM n-dodecyl-B-D-maltoside (DDM), and 5 mM cholesteryl hemisuccinate (CHS) with the protease inhibitor mixture used above] and extracted for 1 hour at 4°C. The solution was clarified by centrifugation (12,000*g* × 10 min) and incubated with CoTALON resins at 4°C for 1 hour, at which point the mixture was transferred to an empty disposable column (Econo-Pac, Bio-Rad). The resin was washed with 10 column volume of buffer A [50 mM tris (pH 7.5), 150 mM KCl, 1 mM DDM, 0.1 mM CHS, and porcine brain total lipid extract (0.1 mg/ml)] with 10 mM imidazole, and bound proteins were eluted with buffer A with 250 mM imidazole. The eluate was concentrated using Amicon Ultra (100 kDa) to ~350 to 450 µl and loaded onto a Superose6 (10 mm by 300 mm) gel filtration column and separated with buffer A. All purification steps described above were carried out at 4°C or on ice.

Lipid nanodisc reconstitution of WT Shaker Kv channels

Lipid nanodisc reconstitution was performed following the previously published methods with minor modifications (*46*). On the day of nanodisc reconstitution, the WT Shaker Kv channel purified by Superose6 in detergent was concentrated to ~1 to 3 mg/ml and incubated with histidine-tagged MSP1E3D1 and 3:1:1 mixture of 1-palmitoyl-2-oleoyl-*sn*-glycero-3-phosphocholine (POPC), 1-palmitoyl-2-oleoyl-sn-glycero-3-phospho-(1′-rac-glycerol) (POPG), and 1-palmitoyl-2-oleoyl-*sn*-glycero-3-phosphoethanolamine (POPE) for 30 min at room temperature. Typically, optimal reconstitution required the incubation of 1:10:200 or 1:10:400 molar ratio of tetrameric WT Shaker Kv channels, MSP1E3D1, and the lipid mixture. The mixture was transferred to a tube with Biobeads (~30- to 50-fold of detergent; w/w) and incubated at room temperature for ~3 hours in the presence of TEV protease (prepared in-house) and 2 mM TCEP to remove N-terminal fusion protein including polyhistidine and mVenus tag. In initial experiments, the reconstituted protein was loaded onto Superose6 column (10 mm by 300 mm) and separated using high-K^+ buffer [20 mM tris-Cl (pH 7.5) and 150 mM KCl]. On the basis of the preliminary cryo-EM data, which indicated comparable conformation between WT Shaker and Shaker-IR, we then prepared a sample using a buffer containing low K^+ and lower ionic strength [20 mM tris-Cl (pH 7.5), 4 mM KCl, and 46 mM NaCl] as these conditions have been shown to promote both C-type and N-type inactivation (*24*, *56*). Successful nanodisc reconstitution was confirmed by collecting separated fractions and running SDS–polyacrylamide gel electrophoresis to verify the presence of WT Shaker Kv channel and MSP1E3D1 bands at a similar ratio.

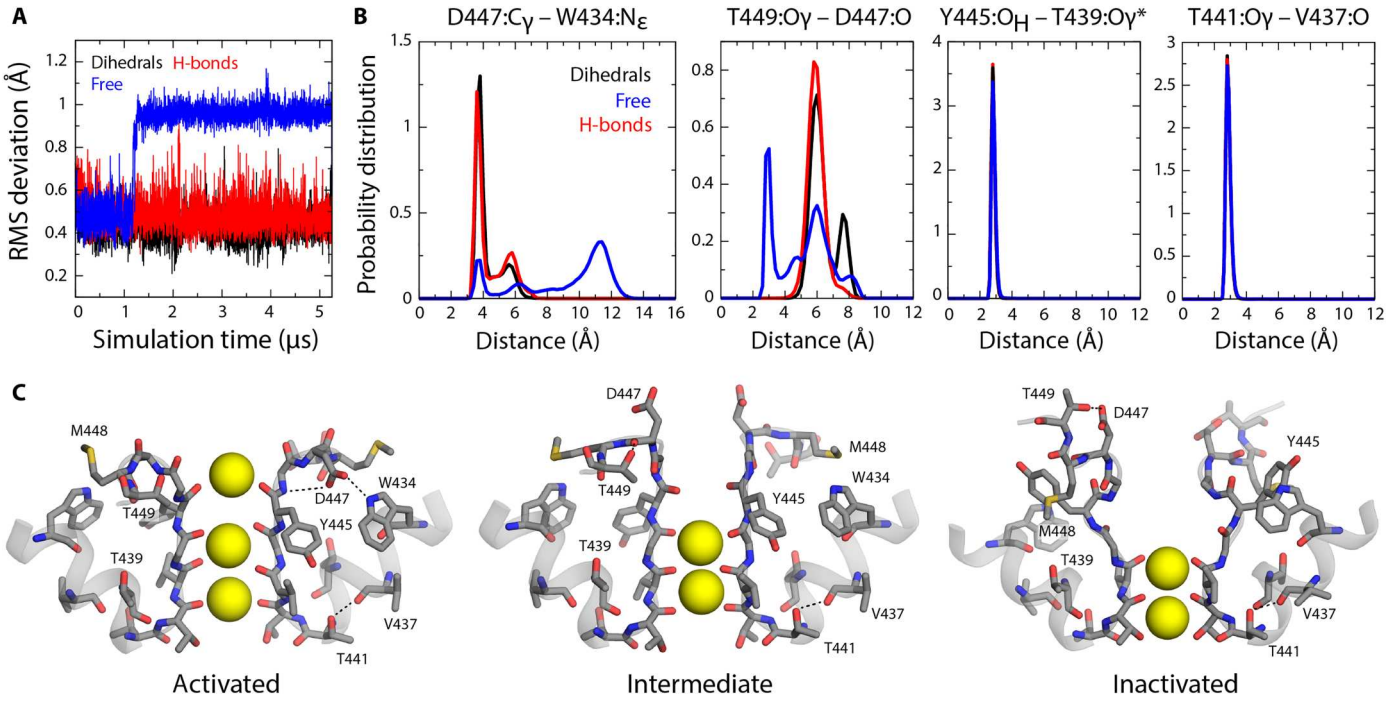

Fig. 8. Competing interaction patterns involving D447 and T449 initiate C-type inactivation. (**A**) RMS differences between the configuration of the selectivity filter in the activated-state cryo-EM structure and trajectory snapshots in three different simulations: (black) one in which weak biasing potentials are applied to all ϕ, ψ, and χ_1 dihedral angles, to loosely maintain the experimental geometry (fig. S3); (blue) another in which the ϕ, ψ, and χ_1 bias is removed for the residues in the selectivity filter (but not the rest of the channel); and (red) another in which ϕ, ψ, and χ_1 bias is removed for the residues in the selectivity filter, but the following hydrogen bonding interactions are preserved: D447 to W434, T441 to V437, and T439 to Y445 (Materials and Methods). (**B**) Hydrogen bonding interactions behind the selectivity filter, examined through probability histograms of the distance between the interacting groups. Data are shown for the three simulations described in (A). Left shifts indicate the formation of an interaction; right shifts indicate a disengagement. (**C**) Snapshots of the simulations of WT Shaker in the activated and inactivated states are contrasted with a snapshot of the conformational intermediate observed when the selectivity filter is permitted to change conformation freely. The molecular system is represented as in Fig. 3 (with K^+ ions in yellow).

Cryo-EM sample preparation and data acquisition

Concentrated samples of WT Shaker in nanodiscs (3 μl) were applied to glow-discharged Quantifoil grids (R 1.2/1.3 Cu 300 mesh). The grids were blotted for 2.5 s, blot force 4, 100% humidity, at 16°C using a FEI Vitrobot Mark IV (Thermo Fisher Scientific), followed by plunging into liquid ethane cooled by liquid nitrogen. Images were acquired using an FEI Titan Krios equipped with a Gatan LS image energy filter (slit width, 20 eV) operating at 300 kV. A Gatan K3 Summit direct electron detector was used to record movies in super-resolution mode with a nominal magnification of ×105,000, resulting in a calibrated pixel size of 0.415 Å per pixel. The typical defocus values ranged from −0.5 to −1.5 μm. Exposures of 1.6 s were dose-fractionated into 32 frames, resulting in a total dose of 52 e^- $Å^{-2}$. Images were recorded using the automated acquisition program SerialEM (*57*).

Image processing

All processing was completed in RELION (*58*). The beam-induced image motion between frames of each dose-fractionated micrograph was corrected and binned by 2 using MotionCor2 (*59*), and contrast transfer function (CTF) estimation was performed using CTFFIND4 (*60*). Micrographs were selected, and those with outliers in defocus value and astigmatism, as well as low resolution (>5 Å) reported by CTFFIND4, were removed. The initial set of particles from 300 micrographs were picked using Gautomatch (www2.mrc-lmb.cam.ac.uk/download/gautomatch-053/) and followed by reference-free two-dimensional (2D) classification in RELION. The good classes were then used as template to pick particles from all selected micrographs using Gautomatch. A total of 15,316,714 particles were picked and extracted with 2× downscaling (pixel size, 1.66 Å). Several rounds of reference-free 2D classification were performed to remove ice spot, contaminants and bad particles, yielding 5,045,482 particles. The good particles were 3D-classified using reference generated by an initial 3D model in C1 symmetry. The good class which did not show the density of ball peptide was selected. After removing duplicate particles, the selected particles were re-extracted using a box size of 300 pixels without binning (pixel size, 0.83 Å). To get good reconstruction within the transmembrane domain, the re-extracted particles were further 3D-classified with a transmembrane domain mask in C4 symmetry, followed by 3D autorefine and CTF refinement. After that, Bayesian polishing was performed, and bad particles were removed from polishing particles using 2D classification. The selected polishing particles were subjected to 3D autorefine in RELION. The final reconstruction was reported at 2.39 Å.

Model building and structure refinement

Model building was first carried out by manually fitting the transmembrane domain of Shaker W434F [Protein Data Bank (PDB) 7SJ1] into the electron microscopy density map using UCSF

Chimera (*61*). The model was then manually built in Coot (*62*) and refined using real_space refinement in PHENIX (*63*) with secondary structure and geometry restraints. The final model was evaluated by comprehensive validation in PHENIX. Structural figures were generated using PyMOL (https://pymol.org/2/support.html) and UCSF Chimera.

MD simulations of outward ion flow under an applied voltage

The simulations of activated WT Shaker and of the inactivated W434F mutant are based on previously reported cryo-EM structures [PDB entries 7SIP (*40*) and 7SJ1 (*40*), respectively], which were used as the starting configurations. The starting structure for the simulations of inactivated WT Shaker was that of the W434F mutant, after reversing the mutation; this model is nearly identical to cryo-EM structure reported in this study. In all cases, the simulations examined a construct encompassing residues 382 to 485 (from S4-S5 linker helix to S6 helix), with neutral N and C termini and all ionizable side chains in their default protonation state at pH 7. For the simulations of activated WT Shaker, two K^+ ions were initially positioned in the selectivity filter, one coordinated by residues 442 and 443 and another by residues 444 and 445; a third ion was positioned below the side chain of 442, and two water molecules were modeled between the three ions. For the simulations of inactivated WT and W434F Shaker, K^+ ions were initially positioned between residues 443 and 444 and by residue 442, with a water molecule in between. Note that neither configuration was ultimately the most populated in the resulting trajectories. For all systems, we used Dowser (*64*) to model structural water molecules within the proteins not resolved in the experimental density maps. To complete the initial simulation setup of the experimental cryo-EM structures, all three constructs (including ions and water molecules) were energy-minimized using CHARMM (*65*) and the CHARMM36m force field (*66*–*68*); specifically, the minimization consisted of 250 steps using the steepest-descent algorithm, followed by 250 steps using the conjugate-gradient algorithm.

All channel constructs were simulated in a POPC lipid bilayer flanked by a 300 mM KCl solution, plus counterions that neutralize the net charge of the systems. To generate a molecular model of this membrane/solvent environment, we created a coarse-grained (CG) POPC lipid bilayer in 300 mM KCl in an orthorhombic box of ~90 Å by 90 Å by 100 Å using insane.py (*69*). To equilibrate this CG system, we carried out a 20-μs MD simulation using GROMACS 2018.8 (*70*) and the MARTINI 2.2 force field (*71*, *72*) at constant temperature (303 K) and constant semi-isotropic pressure (1 atm) and with periodic boundary conditions. The integration time step was 20 fs. We then embedded the structure of activated WT Shaker in this environment; to do so, the atomic structure of the channel was first CG with martinize.py (*71*) and overlaid onto the equilibrated membrane/solvent system, removing all overlapping lipid and water molecules. Then, to optimize the resulting protein/lipid/solvent interfaces, we carried out a 10-μs MD simulation of the complete system using GROMACS 2018.8 (*70*) and MARTINI 2.2 (*71*, *72*) at constant temperature (303 K) and constant semi-isotropic pressure (1 atm) and with periodic boundary conditions and an integration time step of 20 fs. Having ascertained the equilibration of the membrane structure and of the position and orientation of the protein in the lipid bilayer, the final snapshot of the CG trajectory was transformed into an all-atom representation compatible with the all-atom CHARMM36m force field (*66*–*68*). To do so, lipid and solvent molecules were back-mapped (*73*) onto all-atom models, while the CG version of activated WT Shaker was replaced (not back-mapped) with the energy-minimized all-atom construct described above, after optimally superposing the Cα trace of the latter onto that of the former. The resulting all-atom molecular system includes 201 POPC lipids, 14,397 water molecules, and 79 K^+ and 79 Cl^- (300 mM KCl) in an orthorhombic box of ca. 90 Å by 90 Å by 100 Å. To further optimize this all-atom model, the simulation system was first energy-minimized for 5000 steps with NAMD 2.13 (*74*, *75*) and CHARMM36m (*66*–*68*), using the conjugate-gradient algorithm. We then carried out a series of MD simulations wherein structural restraints are applied to the protein and ions/water in the selectivity filter progressively weakened over the course of ~150 ns. The scheme followed in this multistep equilibration is summarized in table S2. These simulations were carried out using NAMD 2.13 (*74*, *75*) and CHARMM36m (*66*–*68*) at constant temperature (298 K) and constant semi-isotropic pressure (1 atm) with periodic boundary conditions and an integration time step of 2 fs. Electrostatic interactions were calculated using Particle-Mesh-Ewald (PME), with a real-space cutoff value of 12 Å; van der Waals interactions were also cut off at 12 Å, with a smooth switching function taking effect at 10 Å.

To construct all-atom simulation systems for the inactivated states, we replaced the structure of activated WT Shaker with those of inactivated WT and W434F at the end of step 6 in the equilibration protocol summarized in table S2. The resulting all-atom molecular systems each includes 201 POPC lipids, 14,383 water molecules, and 79 K^+ and 79 Cl^- (300 mM KCl) in an orthorhombic box of ca. 90 Å by 90 Å by 100 Å. The complete minimization/equilibration protocol (steps 1 through 9) was then repeated for both systems. No external electric field was applied during any of the equilibrations and so the transmembrane voltage in all cases was zero. The dimensions of the simulation systems at the end of the equilibration protocol are ca. 89 Å by 89 Å by 92 Å.

To quantify the ion-conducting properties of activated and inactivated WT Shaker as well as inactivated W434F, multiple 10.5-μs MD trajectories were calculated under an applied voltage (positive inside) using an ANTON2 supercomputer (*76*) and the all-atom CHARMM36m force field (*66*–*68*). The starting configuration for each of these simulations was the final configuration of step 9 in the corresponding equilibration (table S2). To preclude large-scale structural changes in the channel that might develop in the 10-μs timescale due to truncation of the voltage sensors, or cumulative force field inaccuracies, the simulation energy function was supplemented with a weak biasing potential acting on all ϕ, ψ, and χ_1 dihedral angles of the form

$$U(\theta_t) = k\sum_{m=1}^{m=6}(-1)^m\,\{1+\cos[m\theta_t - m(\theta_{\mathrm{exp}t} - 180)]\}/m!$$

where θ_t is the value of each dihedral angle at time t in the simulation, $\theta_{\mathrm{exp}t}$ denotes the corresponding value in the experimental structure, and $k = 1\ k_BT$. This term is identical to that used in previous studies based on microsecond simulations calculated on ANTON platforms (*77*–*79*), except that the magnitude of the bias in this study is considerably weaker (smaller k). Further details are provided in fig. S3.

For activated WT Shaker, two simulations were calculated in symmetric 300 mM KCl: one in which a voltage jump from 0 to 100 mV was introduced at time point 0.5 μs and sustained thereafter, and another in which the voltage jump was from 0 to 300 mV, at the same time point. For inactivated WT and W434F in 300 mM KCl, voltage jumps from 0 to 300 mV and from 300 to 450 mV were introduced at time points 0.5 and 2 μs, respectively. In all cases, the desired transmembrane voltage resulted from application of an outwardly directed, constant electric field perpendicularly to the membrane plane. For a simulation box of approximately 92 Å in that direction, voltages of 100, 300, and 450 mV correspond to electric field magnitudes of 0.025, 0.075, and 0.1125 kcal mol^{-1} Å^{-1} e^{-1}, respectively (note that 1 kcal mol^{-1} Å$^{-1}e^{-1}$ = 43.4 mV/Å). Additional simulations were carried out to examine the competition between K^+ and Na^+. Specifically, for activated and inactivated WT Shaker, the trajectories obtained at 300 mV in 300 mM KCl, as described above, were extended for 10 μs upon exchange of the buffer to 150 mM KCl and 150 NaCl (by redefining 40 randomly selected K^+ ions in solution as Na^+); the transmembrane voltage was maintained at 300 mV. Last, two additional 5-μs trajectories were calculated for activated WT Shaker at 300 mV in 300 mM KCl in which the abovementioned biasing potential acting on ϕ, ψ, and χ_1 dihedral angles was removed for residues 440 to 447 in all subunits, i.e., the selectivity filter and flanking residues. In one trajectory, this region was permitted to evolve freely (according to the force field); in the other, a series of distance restraints were applied instead between the following atom pairs, in all subunits: D447:Cγ and W434:Nε, T441:Oγ and V437:O, and T439:Oγ and Y4450:O_H. The form of these restraints is flat-bottom harmonic potential, i.e.,

$$U(d_t) = 0.5\ k\ (d_t - d_{\mathrm{expt}})^2 \text{ if } d_t > d_{\mathrm{expt}}$$

$$U(d_t) = 0 \text{ if } d_t \leq d_{\mathrm{expt}}$$

where d_t is the distance between the interacting groups at time t in the simulation, d_{expt} denotes the corresponding value in the experimental structure, and k = 100 kcal/mol/Å.

All ANTON2 simulations were carried out at constant temperature (298 K) and semi-isotropic pressure (1 atm), set with the Nose-Hoover thermostat (*80*, *81*) and the Martyna-Tobias-Klein barostat (*82*), respectively, and with periodic boundary conditions and an integration time step of 2.5 fs. Electrostatic interactions were calculated using the Gaussian-split Ewald method (*83*); van der Waals interactions were cut off at 10 Å. No osmotic pressure gradients were applied in any of the ANTON2 or NAMD simulations.

Supplementary Materials

This PDF file includes:
Legends for movies S1 to S5
Figs. S1 to S4
Tables S1 and S2

Other Supplementary Material for this manuscript includes the following:
Movies S1 to S5

REFERENCES AND NOTES

1. G. Yellen, The voltage-gated potassium channels and their relatives. *Nature* **419**, 35–42 (2002).
2. L. Y. Jan, Y. N. Jan, Voltage-gated potassium channels and the diversity of electrical signalling. *J. Physiol.* **590**, 2591–2599 (2012).
3. G. Yellen, The moving parts of voltage-gated ion channels. *Q. Rev. Biophys.* **31**, 239–295 (1998).
4. K. J. Swartz, Sensing voltage across lipid membranes. *Nature* **456**, 891–897 (2008).
5. F. Bezanilla, How membrane proteins sense voltage. *Nat. Rev. Mol. Cell Biol.* **9**, 323–332 (2008).
6. S. B. Long, X. Tao, E. B. Campbell, R. MacKinnon, Atomic structure of a voltage-dependent K^+ channel in a lipid membrane-like environment. *Nature* **450**, 376–382 (2007).
7. W. N. Zagotta, T. Hoshi, R. W. Aldrich, Restoration of inactivation in mutants of *Shaker* potassium channels by a peptide derived from ShB. *Science* **250**, 568–571 (1990).
8. T. Hoshi, W. N. Zagotta, R. W. Aldrich, Biophysical and molecular mechanisms of *Shaker* potassium channel inactivation. *Science* **250**, 533–538 (1990).
9. S. D. Demo, G. Yellen, The inactivation gate of the *Shaker* K^+ channel behaves like an open-channel blocker. *Neuron* **7**, 743–753 (1991).
10. M. Zhou, J. H. Morais-Cabral, S. Mann, R. MacKinnon, Potassium channel receptor site for the inactivation gate and quaternary amine inhibitors. *Nature* **411**, 657–661 (2001).
11. T. Hoshi, W. N. Zagotta, R. W. Aldrich, Two types of inactivation in *Shaker* K^+ channels: Effects of alterations in the carboxy-terminal region. *Neuron* **7**, 547–556 (1991).
12. J. P. Adelman, C. T. Bond, M. Pessia, J. Maylie, Episodic ataxia results from voltage-dependent potassium channels with altered functions. *Neuron* **15**, 1449–1454 (1995).
13. C. A. Hubner, T. J. Jentsch, Ion channel diseases. *Hum. Mol. Genet.* **11**, 2435–2445 (2002).
14. H. T. Kurata, D. Fedida, A structural interpretation of voltage-gated potassium channel inactivation. *Prog. Biophys. Mol. Biol.* **92**, 185–208 (2006).
15. T. Hoshi, C. M. Armstrong, C-type inactivation of voltage-gated K^+ channels: Pore constriction or dilation? *J. Gen. Physiol.* **141**, 151–160 (2013).
16. P. L. Smith, T. Baukrowitz, G. Yellen, The inward rectification mechanism of the HERG cardiac potassium channel. *Nature* **379**, 833–836 (1996).
17. M. T. Keating, M. C. Sanguinetti, Molecular and cellular mechanisms of cardiac arrhythmias. *Cell* **104**, 569–580 (2001).
18. J. M. Nerbonne, R. S. Kass, Molecular physiology of cardiac repolarization. *Physiol. Rev.* **85**, 1205–1253 (2005).
19. M. C. Sanguinetti, M. Tristani-Firouzi, hERG potassium channels and cardiac arrhythmia. *Nature* **440**, 463–469 (2006).
20. J. Yan, Q. Li, R. W. Aldrich, Closed state-coupled C-type inactivation in BK channels. *Proc. Natl. Acad. Sci. U.S.A.* **113**, 6991–6996 (2016).
21. M. Schewe, H. Sun, Ü. Mert, A. Mackenzie, A. C. W. Pike, F. Schulz, C. Constantin, K. S. Vowinkel, L. J. Conrad, A. K. Kiper, W. Gonzalez, M. Musinszki, M. Tegtmeier, D. C. Pryde, H. Belabed, M. Nazare, B. L. de Groot, N. Decher, B. Fakler, E. P. Carpenter, S. J. Tucker, T. Baukrowitz, A pharmacological master key mechanism that unlocks the selectivity filter gate in K^+ channels. *Science* **363**, 875–880 (2019).
22. K. L. Choi, R. W. Aldrich, G. Yellen, Tetraethylammonium blockade distinguishes two inactivation mechanisms in voltage-activated K^+ channels. *Proc. Natl. Acad. Sci. U.S.A.* **88**, 5092–5095 (1991).
23. E. Perozo, R. MacKinnon, F. Bezanilla, E. Stefani, Gating currents from a nonconducting mutant reveal open-closed conformations in *Shaker* K^+ channels. *Neuron* **11**, 353–358 (1993).
24. J. Lopez-Barneo, T. Hoshi, S. H. Heinemann, R. W. Aldrich, Effects of external cations and mutations in the pore region on C-type inactivation of *Shaker* potassium channels. *Recept. Channels* **1**, 61–71 (1993).
25. G. Yellen, D. Sodickson, T. Y. Chen, M. E. Jurman, An engineered cysteine in the external mouth of a K^+ channel allows inactivation to be modulated by metal binding. *Biophys. J.* **66**, 1068–1075 (1994).
26. T. Baukrowitz, G. Yellen, Modulation of K^+ current by frequency and external [K^+]: A tale of two inactivation mechanisms. *Neuron* **15**, 951–960 (1995).
27. Y. Liu, M. E. Jurman, G. Yellen, Dynamic rearrangement of the outer mouth of a K^+ channel during gating. *Neuron* **16**, 859–867 (1996).
28. Y. Yang, Y. Yan, F. J. Sigworth, The Shaker mutation T449V rescues ionic currents of W434F K^+ channels. *Biophys. J.* **82**, 234e (2002).
29. Y. Yang, Y. Yan, F. J. Sigworth, How does the W434F mutation block current in *Shaker* potassium channels? *J. Gen. Physiol.* **109**, 779–789 (1997).
30. J. G. Starkus, L. Kuschel, M. D. Rayner, S. H. Heinemann, Ion conduction through C-type inactivated *Shaker* channels. *J. Gen. Physiol.* **110**, 539–550 (1997).

31. A. Molina, A. G. Castellano, J. Lopez-Barneo, Pore mutations in Shaker K+ channels distinguish between the sites of tetraethylammonium blockade and C-type inactivation. *J. Physiol.* **499**(Pt 2), 361–367 (1997).
32. E. M. Ogielska, R. W. Aldrich, A mutation in S6 of *Shaker* potassium channels decreases the K^+ affinity of an ion binding site revealing ion-ion interactions in the pore. *J. Gen. Physiol.* **112**, 243–257 (1998).
33. E. M. Ogielska, R. W. Aldrich, Functional consequences of a decreased potassium affinity in a potassium channel pore. Ion interactions and C-type inactivation. *J. Gen. Physiol.* **113**, 347–358 (1999).
34. C. M. Armstrong, T. Hoshi, K^+ channel gating: C-type inactivation is enhanced by calcium or lanthanum outside. *J. Gen. Physiol.* **144**, 221–230 (2014).
35. L. G. Cuello, D. M. Cortes, E. Perozo, The gating cycle of a K^+ channel at atomic resolution. *eLife* **6**, e28032 (2017).
36. L. G. Cuello, V. Jogini, D. M. Cortes, E. Perozo, Structural mechanism of C-type inactivation in K^+ channels. *Nature* **466**, 203–208 (2010).
37. L. G. Cuello, V. Jogini, D. M. Cortes, A. C. Pan, D. G. Gagnon, O. Dalmas, J. F. Cordero-Morales, S. Chakrapani, B. Roux, E. Perozo, Structural basis for the coupling between activation and inactivation gates in K^+ channels. *Nature* **466**, 272–275 (2010).
38. S. A. Pless, J. D. Galpin, A. P. Niciforovic, H. T. Kurata, C. A. Ahern, Hydrogen bonds as molecular timers for slow inactivation in voltage-gated potassium channels. *eLife* **2**, e01289 (2013).
39. F. Bezanilla, Gating currents. *J. Gen. Physiol.* **150**, 911–932 (2018).
40. X.-F. Tan, C. Bae, R. Stix, A. I. Fernández-Mariño, K. Huffer, T.-H. Chang, J. Jiang, J. D. Faraldo-Gómez, K. J. Swartz, Structure of the Shaker Kv channel and mechanism of slow C-type inactivation. *Sci. Adv.* **8**, eabm7814 (2022).
41. M. Lolicato, A. M. Natale, F. Abderemane-Ali, D. Crottès, S. Capponi, R. Duman, A. Wagner, J. M. Rosenberg, M. Grabe, D. L. Minor Jr., K_{2P} channel C-type gating involves asymmetric selectivity filter order-disorder transitions. *Sci. Adv.* **6**, eabc9174 (2020).
42. R. Reddi, K. Matulef, E. A. Riederer, M. R. Whorton, F. I. Valiyaveetil, Structural basis for C-type inactivation in a Shaker family voltage-gated K^+ channel. *Sci. Adv.* **8**, eabm8804 (2022).
43. P. Selvakumar, A. I. Fernández-Mariño, N. Khanra, C. He, A. J. Paquette, B. Wang, R. Huang, V. V. Smider, W. J. Rice, K. J. Swartz, J. R. Meyerson, Structures of the T cell potassium channel Kv1.3 with immunoglobulin modulators. *Nat. Commun.* **13**, 3854 (2022).
44. A. Tyagi, T. Ahmed, S. Jian, S. Bajaj, S. T. Ong, S. S. M. Goay, Y. Zhao, I. Vorobyov, C. Tian, K. G. Chandy, S. Bhushan, Rearrangement of a unique Kv1.3 selectivity filter conformation upon binding of a drug. *Proc. Natl. Acad. Sci. U.S.A.* **119**, e2113536119 (2022).
45. L. Coonen, E. Martinez-Morales, D. V. van de Sande, D. J. Snyders, D. M. Cortes, L. G. Cuello, A. J. Labro, The nonconducting W434F mutant adopts upon membrane depolarization an inactivated-like state that differs from wild-type Shaker-IR potassium channels. *Sci. Adv.* **8**, eabn1731 (2022).
46. D. Matthies, C. Bae, G. E. S. Toombes, T. Fox, A. Bartesaghi, S. Subramaniam, K. J. Swartz, Single-particle cryo-EM structure of a voltage-activated potassium channel in lipid nanodiscs. *eLife* **7**, e37558 (2018).
47. Y. Liu, M. Holmgren, M. E. Jurman, G. Yellen, Gated access to the pore of a voltage-dependent K^+ channel. *Neuron* **19**, 175–184 (1997).
48. Y. Zhou, J. H. Morais-Cabral, A. Kaufman, R. MacKinnon, Chemistry of ion coordination and hydration revealed by a K^+ channel–Fab complex at 2.0 Å resolution. *Nature* **414**, 43–48 (2001).
49. L. Heginbotham, R. MacKinnon, Conduction properties of the cloned Shaker K^+ channel. *Biophys. J.* **65**, 2089–2096 (1993).
50. A. Mironenko, U. Zachariae, B. L. de Groot, W. Kopec, The persistent question of potassium channel permeation mechanisms. *J. Mol. Biol.* **433**, 167002 (2021).
51. D. A. Kopfer, C. Song, T. Gruene, G. N. Sheldrick, U. Zachariae, B. L. de Groot, Ion permeation in K^+ channels occurs by direct Coulomb knock-on. *Science* **346**, 352–355 (2014).
52. W. Kopec, D. A. Köpfer, O. N. Vickery, A. S. Bondarenko, T. L. C. Jansen, B. L. de Groot, U. Zachariae, Direct knock-on of desolvated ions governs strict ion selectivity in K^+ channels. *Nat. Chem.* **10**, 813–820 (2018).
53. T. Kitaguchi, M. Sukhareva, K. J. Swartz, Stabilizing the closed S6 gate in the Shaker K_v channel through modification of a hydrophobic seal. *J. Gen. Physiol.* **124**, 319–332 (2004).
54. M. S. Rana, X. Wang, A. Banerjee, An improved strategy for fluorescent tagging of membrane proteins for overexpression and purification in mammalian cells. *Biochemistry* **57**, 6741–6751 (2018).
55. A. Goehring, C.-H. Lee, K. H. Wang, J. C. Michel, D. P. Claxton, I. Baconguis, T. Althoff, S. Fischer, K. C. Garcia, E. Gouaux, Screening and large-scale expression of membrane proteins in mammalian cells for structural studies. *Nat. Protoc.* **9**, 2574–2585 (2014).
56. R. D. Murrell-Lagnado, R. W. Aldrich, Energetics of Shaker K channels block by inactivation peptides. *J. Gen. Physiol.* **102**, 977–1003 (1993).
57. D. N. Mastronarde, Automated electron microscope tomography using robust prediction of specimen movements. *J. Struct. Biol.* **152**, 36–51 (2005).
58. J. Zivanov, T. Nakane, B. O. Forsberg, D. Kimanius, W. J. Hagen, E. Lindahl, S. H. Scheres, New tools for automated high-resolution cryo-EM structure determination in RELION-3. *eLife* **7**, e42166 (2018).
59. S. Q. Zheng, E. Palovcak, J.-P. Armache, K. A. Verba, Y. Cheng, D. A. Agard, MotionCor2: Anisotropic correction of beam-induced motion for improved cryo-electron microscopy. *Nat. Methods* **14**, 331–332 (2017).
60. A. Rohou, N. Grigorieff, CTFFIND4: Fast and accurate defocus estimation from electron micrographs. *J. Struct. Biol.* **192**, 216–221 (2015).
61. E. F. Pettersen, T. D. Goddard, C. C. Huang, G. S. Couch, D. M. Greenblatt, E. C. Meng, T. E. Ferrin, UCSF Chimera–A visualization system for exploratory research and analysis. *J. Comput. Chem.* **25**, 1605–1612 (2004).
62. P. Emsley, B. Lohkamp, W. G. Scott, K. Cowtan, Features and development of *Coot*. *Acta Crystallogr. D Biol. Crystallogr.* **66**(Pt 4), 486–501 (2010).
63. P. D. Adams, P. V. Afonine, G. Bunkóczi, V. B. Chen, I. W. Davis, N. Echols, J. J. Headd, L. W. Hung, G. J. Kapral, R. W. Grosse-Kunstleve, A. J. McCoy, N. W. Moriarty, R. Oeffner, R. J. Read, D. C. Richardson, J. S. Richardson, T. C. Terwilliger, P. H. Zwart, *PHENIX*: A comprehensive Python-based system for macromolecular structure solution. *Acta Crystallogr. D Biol. Crystallogr.* **66**(Pt 2), 213–221 (2010).
64. L. Zhang, J. Hermans, Hydrophilicity of cavities in proteins. *Proteins* **24**, 433–438 (1996).
65. B. R. Brooks, C. L. Brooks III, A. D. Mackerell Jr., L. Nilsson, R. J. Petrella, B. Roux, Y. Won, G. Archontis, C. Bartels, S. Boresch, A. Caflisch, L. Caves, Q. Cui, A. R. Dinner, M. Feig, S. Fischer, J. Gao, M. Hodoscek, W. Im, K. Kuczera, T. Lazaridis, J. Ma, V. Ovchinnikov, E. Paci, R. W. Pastor, C. B. Post, J. Z. Pu, M. Schaefer, B. Tidor, R. M. Venable, H. L. Woodcock, X. Wu, W. Yang, D. M. York, M. Karplus, CHARMM: The biomolecular simulation program. *J. Comput. Chem.* **30**, 1545–1614 (2009).
66. J. Huang, S. Rauscher, G. Nawrocki, T. Ran, M. Feig, B. L. de Groot, H. Grubmüller, A. D. MacKerell Jr., CHARMM36m: An improved force field for folded and intrinsically disordered proteins. *Nat. Methods* **14**, 71–73 (2017).
67. R. B. Best, X. Zhu, J. Shim, P. E. M. Lopes, J. Mittal, M. Feig, A. D. MacKerell Jr., Optimization of the additive CHARMM all-atom protein force field targeting improved sampling of the backbone ϕ, ψ and side-chain χ1and χ2 Dihedral angles. *J. Chem. Theory Comput.* **8**, 3257–3273 (2012).
68. J. B. Klauda, R. M. Venable, J. A. Freites, J. W. O'Connor, D. J. Tobias, C. Mondragon-Ramirez, I. Vorobyov, A. D. MacKerell Jr., R. W. Pastor, Update of the CHARMM all-atom additive force field for lipids: Validation on six lipid types. *J. Phys. Chem. B* **114**, 7830–7843 (2010).
69. T. A. Wassenaar, H. I. Ingolfsson, R. A. Bockmann, D. P. Tieleman, S. J. Marrink, Computational lipidomics with *insane*: A versatile tool for generating custom membranes for molecular simulations. *J. Chem. Theory Comput.* **11**, 2144–2155 (2015).
70. S. Pronk, S. Páll, R. Schulz, P. Larsson, P. Bjelkmar, R. Apostolov, M. R. Shirts, J. C. Smith, P. M. Kasson, D. van der Spoel, B. Hess, E. Lindahl, GROMACS 4.5: A high-throughput and highly parallel open source molecular simulation toolkit. *Bioinformatics* **29**, 845–854 (2013).
71. D. H. de Jong, G. Singh, W. F. D. Bennett, C. Arnarez, T. A. Wassenaar, L. V. Schäfer, X. Periole, D. P. Tieleman, S. J. Marrink, Improved parameters for the martini coarse-grained protein force field. *J. Chem. Theory Comput.* **9**, 687–697 (2013).
72. S. J. Marrink, H. J. Risselada, S. Yefimov, D. P. Tieleman, A. H. de Vries, The MARTINI force field: Coarse grained model for biomolecular simulations. *J. Phys. Chem. B* **111**, 7812–7824 (2007).
73. T. A. Wassenaar, K. Pluhackova, R. A. Bockmann, S. J. Marrink, D. P. Tieleman, Going backward: A flexible geometric approach to reverse transformation from coarse grained to atomistic models. *J. Chem. Theory Comput.* **10**, 676–690 (2014).
74. J. C. Phillips, D. J. Hardy, J. D. C. Maia, J. E. Stone, J. V. Ribeiro, R. C. Bernardi, R. Buch, G. Fiorin, J. Hénin, W. Jiang, R. McGreevy, M. C. R. Melo, B. K. Radak, R. D. Skeel, A. Singharoy, Y. Wang, B. Roux, A. Aksimentiev, Z. Luthey-Schulten, L. V. Kalé, K. Schulten, C. Chipot, E. Tajkhorshid, Scalable molecular dynamics on CPU and GPU architectures with NAMD. *J. Chem. Phys.* **153**, 044130 (2020).
75. G. Fiorin, M. L. Klein, J. Henin, Using collective variables to drive molecular dynamics simulations. *Mol. Phys.* **111**, 3345–3362 (2013).
76. D. E. Shaw, J. P. Grossman, J. A. Bank, B. Batson, J. A. Butts, J. C. Chao, M. M. Deneroff, R. O. Dror, A. Even, C. H. Fenton, A. Forte, J. Gagliardo, G. Gill, B. Greskamp, C. R. Ho, D. J. Ierardi, L. Iserovich, J. S. Kuskin, R. H. Larson, T. Layman, L.-S. Lee, A. K. Lerer, C. Li, D. Killebrew, K. M. Mackenzie, S. Y.-H. Mok, M. A. Moraes, R. Mueller, L. J. Nociolo, J. L. Peticolas, T. Quan, D. Ramot, J. K. Salmon, D. P. Scarpazza, U. B. Schafer, N. Siddique, C. W. Snyder, J. Spengler, P. T. P. Tang, M. Theobald, H. Toma, B. Towles, B. Vitale, S. C. Wang, C. Young, paper presented at the SC14: International Conference for High Performance Computing, Networking, Storage and Analysis, New Orleans, LA, USA, 16 to 21 November 2014.

77. A. C. Pan, D. Jacobson, K. Yatsenko, D. Sritharan, T. M. Weinreich, D. E. Shaw, Atomic-level characterization of protein-protein association. *Proc. Natl. Acad. Sci. U.S.A.* **116**, 4244–4249 (2019).
78. M. O. Jensen, V. Jogini, D. W. Borhani, A. E. Leffler, R. O. Dror, D. E. Shaw, Mechanism of voltage gating in potassium channels. *Science* **336**, 229–233 (2012).
79. Y. C. Park, B. Reddy, N. Bavi, E. Perozo, J. D. Faraldo-Gómez, State-specific morphological deformations of the lipid bilayer explain mechanosensitive gating of MscS ion channels. *eLife* **12**, e81445 (2023).
80. S. Nosé, A molecular dynamics method for simulations in the canonical ensemble. *Mol. Phys.* **52**, 255–268 (1984).
81. W. G. Hoover, Canonical dynamics - Equilibrium phase-space distributions. *Phys. Rev. A Gen. Phys.* **31**, 1695–1697 (1985).
82. G. J. Martyna, D. J. Tobias, M. L. Klein, Constant-pressure molecular-dynamics algorithms. *J. Chem. Phys.* **101**, 4177–4189 (1994).
83. Y. Shan, J. L. Klepeis, M. P. Eastwood, R. O. Dror, D. E. Shaw, Gaussian split Ewald: A fast Ewald mesh method for molecular simulation. *J. Chem. Phys.* **122**, 54101 (2005).

Acknowledgments: We thank members of the Swartz laboratory for helpful discussion and H. Wang in the NIH Multi-Institute Cryo-EM Facility (MICEF) for assistance in acquiring cryo-EM data. This work used resources provided by the NIH MICEF, the NIH HPC facility Biowulf the Pittsburgh Supercomputing Center. **Funding:** This research was supported by the Intramural Research Programs of the National Institute of Neurological Disorders and Stroke, NIH, Bethesda, MD to K.J.S. (NS002945) and the National Heart Blood and Lung Institute, NIH, Bethesda, MD to J.D.F.-G. (HL006203). **Author contributions:** Conceptualization: R.S., X.-F.T., K.J.S., and J.D.F.-G. Methodology: R.S., X.-F.T., C.B., A.I.F.-M., K.J.S., and J.D.F.-G. Investigation: R.S., X.-F.T., C.B., A.I.F.-M., K.J.S., and J.D.F.-G. Visualization: R.S., X.-F.T., C.B., A.I.F.-M., K.J.S., and J.D.F.-G. Funding acquisition: K.J.S. and J.D.F.-G. Project administration: K.J.S. and J.D.F.-G. Supervision: K.J.S. and J.D.F.-G. Writing—original draft: R.S., X.-F.T., K.J.S., and J.D.F.-G. Writing—review and editing: R.S., X.-F.T., K.J.S., and J.D.F.-G. **Competing interests:** The authors declare that they have no competing interests. **Data and materials availability:** All data needed to evaluate the conclusions in the paper are present in the paper and/or the Supplementary Materials. The cryo-EM map for C-type inactivated WT Shaker has been deposited in the Electron Microscopy Data Bank with accession code EMD-41193. A structural model has been deposited in the PDB with accession code 8TEO.

Submitted 4 July 2023
Accepted 9 November 2023
Published 8 December 2023
10.1126/sciadv.adj5539